A self-regulated gradient interphase for dendrite-free solid-state Li batteries

Tengrui Wang[1a], Jian Duan[1a], Bao Zhang[2a], Wei Luo[1]*, Xiao Ji[2], Henghui Xu[3], Ying Huang[1], Liqiang Huang[1], Zhenyou Song[1], Jiayun Wen[1], Chunsheng Wang[2]*, Yunhui Huang[1,4]*, John B. Goodenough[3*]

[1]Institute of New Energy for Vehicles, School of Materials Science and Engineering, Tongji University, Shanghai 201804, China

[2]Department of Chemical & Biomolecular Engineering, University of Maryland College Park, College Park, Maryland, 20742, United States

[3]Materials Science and Engineering Program and Department of Mechanical Engineering, The University of Texas at Austin, Austin 78712 TX, USA.

[4]State Key Laboratory of Material Processing and Die & Mould Technology, School of Materials Science and Engineering, Huazhong University of Science and Technology, Wuhan 430074, China

[a] These authors contributed equally.

* Corresponding authors: weiluo@tongji.edu.cn (W.L.); cswang@umd.edu (C.S.W.); jgoodenough@mail.utexas.edu (J.B.G.); huangyh@hust.edu.cn (Y.H.H)

Table of Contents

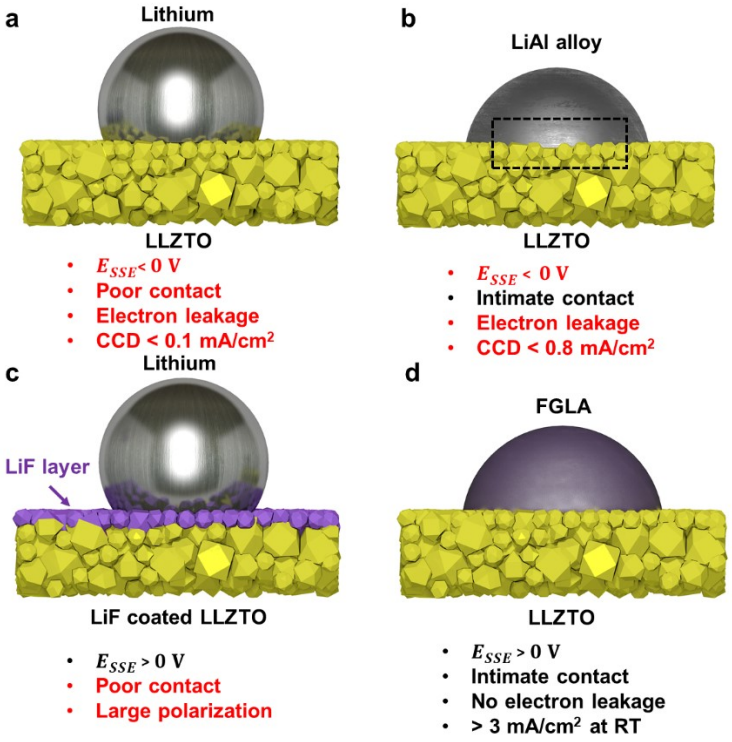

Figure S1. Schematic of the interface between Li metal anode and garnet. (a) Li metal balls up on garnet, exhibiting a poor interface wetting. Dendritic Li and short-circuit occur at a very low CCD, such as 0.1 mA·cm^{-2}, due to the large interfacial resistance and electron leakage upon plating/stripping. (b) Lithiophilic LiAl alloy can significantly improve the contact but electron leakage exists, which finally results in Li dendrite formation at about 0.8 mA·cm^{-2}. (c) Surface coating garnet with a layer of electronically insulating, lithiophobic LiF can prevent garnet from generating Li dendrite inside. Unfortunately, the poor interface wetting leads to a limited contact area and severe battery polarization. (d) Engineering a lithiophilic-lithiophobic FGLA by compositing Li metal with AlF_3 not only offers an intimate contact with garnet, but also suppresses the formation of Li dendrites under a current density up to over 3.0 mA·cm^{-2} at RT.

Fabrication, structural characterization and capacity of FGLA

To fabricate the Li-AlF_3 composites (FGLAs), Li foil was placed in a stainless-steel crucible and heated on a hotplate at 300 °C in a glovebox (concentrations of O_2 and H_2O were lower than 0.1 ppm). Impurities on the surface of molten Li were removed carefully with stainless-steel tweezers. AlF_3 powder (Fig. S2) was weighed according to the Li/AlF_3 mass ratios and added into molten Li. Next, the mixed composites were continuously stirred until all AlF_3 powder disappeared, as shown in Fig. S3. After cooling down to room temperature, Li-AlF_3 composites (FGLAs) with different Li/AlF_3 mass ratios were given.

Digital photos (I) were taken to research the viscosities of the composites and XRD (II) was utilized to investigate the structure of the composites. The specific capacities of different Li-AlF_3 composites (III) were also calculated.

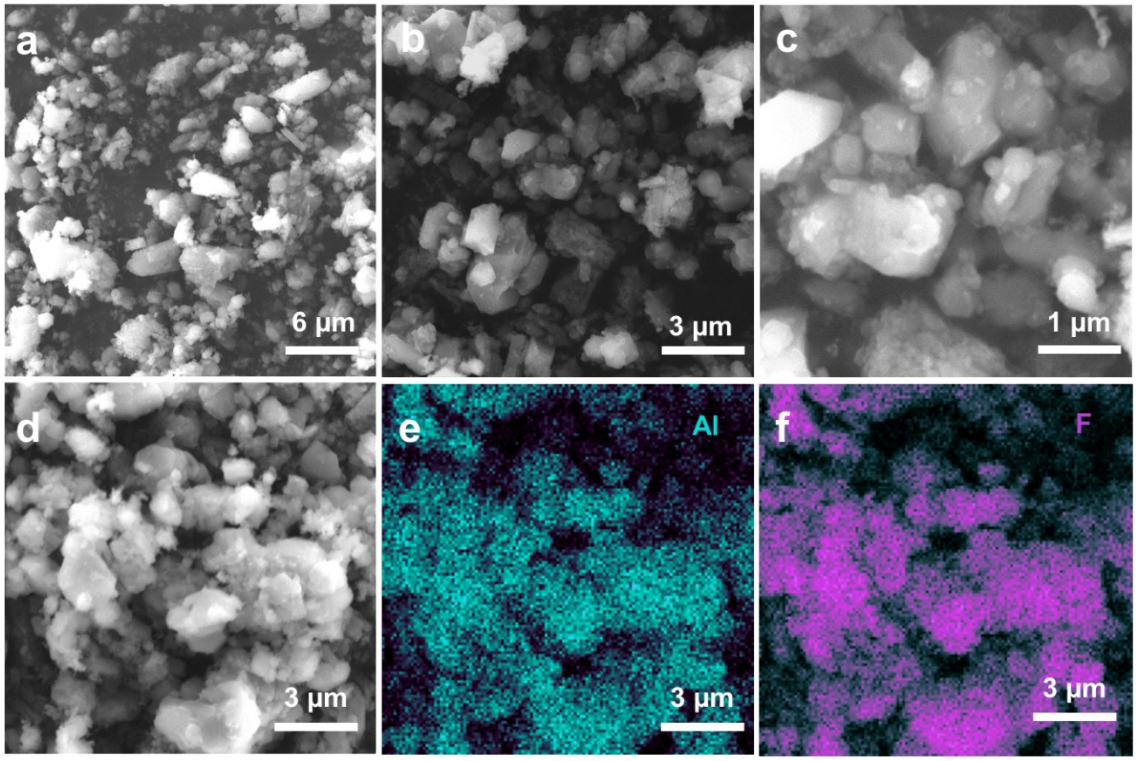

Figure S2. (a-c) SEM and (d-f) EDX mapping images of AlF_3 powder.

Figure S3. The fabrication process of adding AlF_3 into molten Li under stirring at 300 °C. AlF_3 experienced conversion and alloying reactions upon the reaction with molten Li, generating LiF, Li_9Al_4 with excessive Li.

(I) Study the viscosity changes of FGLAs with different Li/AlF_3 mass ratios with digital photos

As illustrated in Fig. S4A, FGLA with a Li/AlF_3 mass ratio of 1:2.30 is solid at 300 °C with unreacted AlF_3 powder, indicating the inhomogeneous and incomplete reactions. To realize homogeneous and complete reactions of Li and AlF_3, the content of lithium was increased. Notably, AlF_3 powder disappears when the Li/AlF_3 mass ratio rises, suggesting the complete reaction of AlF_3. More interestingly, with the increase of Li/AlF_3 mass ratio, the viscosities of the composites tend to decrease. When the Li/AlF_3 mass ratio reaches 2:1, the viscosity of the composite is moderate, which shows an intimate contact with LLZTO in the following experiments. Nevertheless, without adding AlF_3, pure Li balls up in the crucible at 300 ℃, demonstrating its poor wettability.

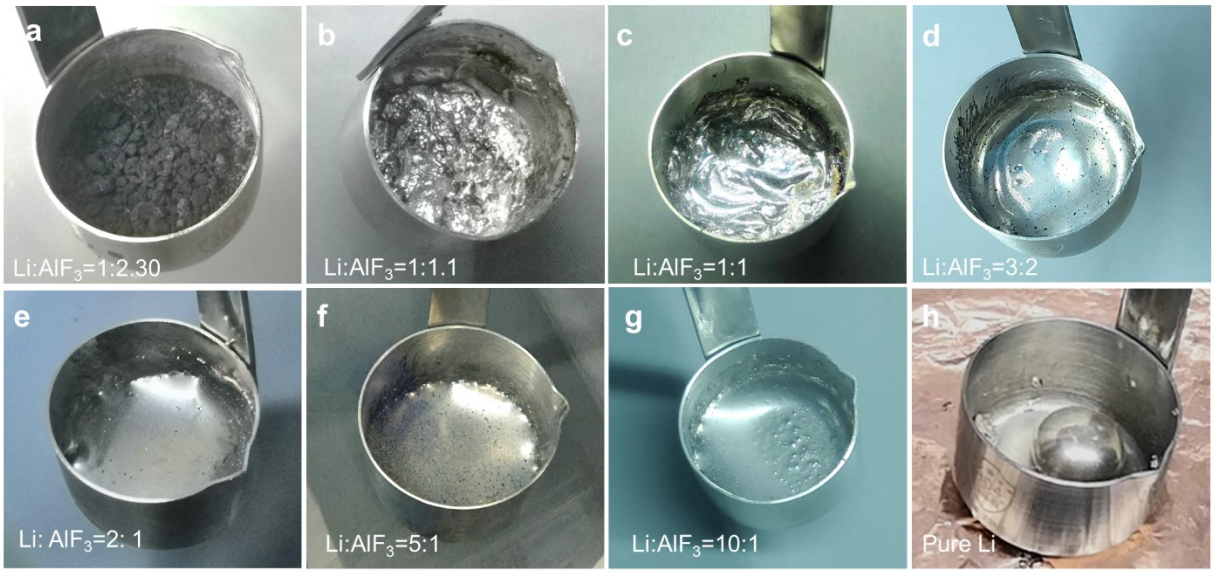

Figure S4. Digital photos of FGLAs with different Li/AlF_3 mass ratios at 300 °C.

(II) XRD patterns of FGLAs with different Li/AlF_3 mass ratios

According to the results of first-principles computation shown in Table S1, the composition of FGLAs mainly depends on Li/AlF_3 mass ratios. Accordingly, the products should only consist of LiF and Li_9Al_4 when the Li/AlF_3 mass ratio reaches 1:2.30. However, peaks of Li_3Al_2 and unreacted AlF_3 (Fig. S5) can be found in the composite, which is consistent with the result of digital photos (Fig. S4). When the Li/AlF_3 mass ratio increases to 1:1, as expected, XRD peaks of AlF_3 powder disappear in the composites, indicating the complete consumption of AlF_3. The reaction products in the composite are Li_9Al_4, LiF and excessive Li. Moreover, with the increase of Li/AlF_3 mass ratios, the relative peak intensities of Li_9Al_4 and LiF decrease, whereas the relative intensities of metallic Li increase. It should be noted that the broad peak near 20° corresponds to the Kapton tape used for XRD measurements

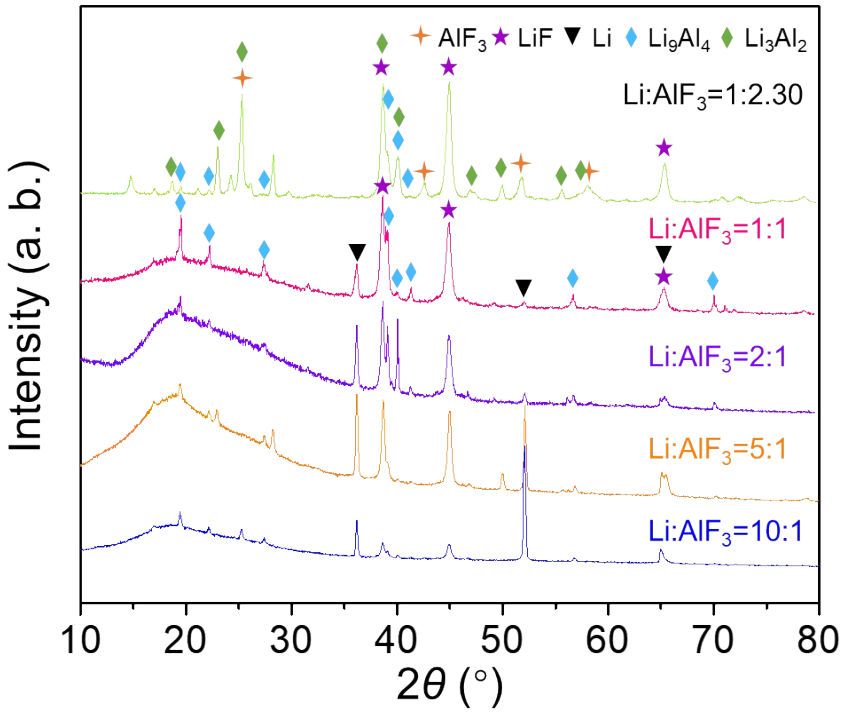

Figure S5. XRD patterns of FGLAs with different Li/AlF_3 mass ratios.

(III) Specific capacity calculation of FGLAs with different Li/AlF_3 mass ratios

The specific capacity is also a crucial characteristic of anode materials. Herein, we calculated the detailed compositions and specific capacities of different FGLAs according to the equation $Q = \frac{nF}{m}$, where Q, n, F and m represented the specific capacity, the transferred electrons per molar (for lithium metal, n=1), the Faraday constant (96485 C/mol) and the molar mass of anode respectively. According to the previous study, we only calculate the capacity based on the excessive Li in the Li-AlF_3 composites as the active mass. For example, the capacity is 0 mAh/g when the Li/AlF_3 mass ratio is 1:2.30 since there is no excessive Li in the composite according to the thermodynamic equation. With increasing the content of Li, the capacity gradually increases. As shown in Table S2, the composite with a Li/AlF_3 mass ratio of 2:1 offers a specific capacity of 2016 mAh/g. When the mass ratio is 10:1, the specific capacity reaches 3356 mAh/g, which is slightly lower than that of pure lithium (3861 mAh/g).

Considering all these characteristics mentioned above, here we chose the composite with a Li/AlF_3 mass ratio of 2:1 to conduct the further research. On the one hand, FGLA with a mass ratio of 2:1 displays a moderate viscosity, which means great wetting performance and good processability. On the other hand, the composite still delivers a relatively high capacity and a high content of LiF.

Supplementary Note 1: Thermodynamic analysis for the phase separation.

Phase separation in the x-Li system (x can be LiF or Li_9Al_4) system

To further clarify this unique and interesting phenomenon, the phase separation of FGLA was thermodynamically analyzed using DFT calculations. In a X-Li binary system where X is the other phase, the internal energy U of this system can be quantified as,

$$U = 0.5n_X \times (\gamma_X + \gamma_{X-Li}) \times s_X + N_X \times \gamma_{X-Li} \times s_X.$$

N_X (N_{Li}) is the number of X (Li) particles within Li and n_X (n_{Li}) is the number of X (Li) on the Li surface. S_X (S_{Li}) is the surface area per X (Li) particle. γ_X is the surface energy of X and $\gamma_{X\text{-}Li}$ is the interfacial energy for X-Li. U is the internal energy and F is the Gibbs free energy of the Li-X system. According to the second law of thermodynamics, considering that the internal energy is equal to the enthalpy for solid materials, $F = U - TS$. T is the absolute temperature. According to Boltzmann equation, $S = k\ln W$, where W is the number of microscopic states of this X-Li system and k is the Boltzmann constant.

$$W = \frac{N!}{N_X!N_{Li}!}\frac{n!}{n_X!n_{Li}!} \quad (N = N_X + N_{Li}, n = n_X + n_{Li})$$

$$F = 0.5n_X \times (\gamma_X + \gamma_{X-Li}) \times s_X + N_X \times \gamma_{X-Li} \times s_X - kT\ln\left(\frac{N!}{N_X!N_{Li}!}\frac{n!}{n_X!n_{Li}!}\right)$$

$$\frac{dF}{dN_X} = -\frac{dF}{dn_X},\ \frac{d\ln W}{dN_X} = \ln\frac{N-N_X}{N_X} - \ln\frac{n-n_X}{n_X} = \ln\left(\frac{N_{Li}n_X}{N_Xn_{Li}}\right)$$

The distribution of X on the surface (n_X) or in the bulk (N_X) of the Li composite depends on the Gibbs free energy. When the Gibbs free energy is minimum, the system is in an equilibrium state. The necessary condition for minimum Gibbs free energy is that its first derivative is equal to 0.

$$\left(\frac{dF}{dn}\right)_T = 0$$

$$\left(\frac{dF}{dn}\right)_T = 0.5\left(\gamma_X + \gamma_{X\text{-}Li}\right) \times s_X - \gamma_{X\text{-}Li} \times s_X + kT\ln\left(\frac{N_{Li}n_X}{N_Xn_{Li}}\right) = 0$$

$$\ln\left(\frac{N_{Li}n_X}{N_Xn_{Li}}\right) = -\frac{0.5(\gamma_X - \gamma_{X-Li}) \times s_X}{kT}$$

$$\frac{n_X}{n_{Li}} = \frac{N_X}{N_{Li}} \times e^{\left(-\frac{0.5(\gamma_X - \gamma_{X-Li}) \times s_X}{kT}\right)}$$

The corresponding surface and interfacial energies are shown in Figure S6. *For LiF*, $\gamma_{LiF} - \gamma_{LiF\text{-}Li} = -0.47\ J/m^2 < 0$

$\frac{n_{LiF}}{n_{Li}} > \frac{N_{LiF}}{N_{Li}}$ *p*hase separation occurs.

LiF tends to concentrate on the surface of Li.

$\gamma_{Li9Al4} - \gamma_{Li9Al4-Li} = 0.826\, J/m^2 > 0$

$\frac{n_{Li9Al4}}{n_{Li}} < \frac{N_{Li9Al4}}{N_{Li}}$.

Li_9Al_4 tends to be in the bulk of Li.

Phase separation in the X-Li-LLZO system (x can be LiF or Li_9Al_4) system

Similar with the formula derivation above,the internal energy U of this system can be quantified as,

$U = 0.5n_X \times (\gamma_{X-Li} + \gamma_{X-LLZO}) \times s_X + N_X \times \gamma_{X-Li} \times s_X$

N_X (N_{Li}) is the number of X (Li) particles within Li and n_X (n_{Li}) is the number of X (Li) on the Li surface. S_X (S_{Li}) is the surface area per X (Li) particle. $\gamma_{X\text{-}Li}$ and $\gamma_{X\text{-}LLZO}$ are the interfacial energies for X-Li and X-LLZO, respectively. U is the internal energy and F is the Gibbs free energy of the system.

$$F = U - TS$$
$$S = k\ln W$$

k and T are the Boltzmann constant and the absolute temperature, respectively.

$$W = \frac{N!}{N_X!N_{Li}!}\frac{n!}{n_X!n_{Li}!} \quad (N = N_X + N_{Li}, n = n_X + n_{Li})$$

$$F = 0.5n_X \times (\gamma_{X-Li} + \gamma_{X-LLZO}) \times s_X + N_X \times \gamma_{X-Li} \times s_X - kT\ln\left(\frac{N!}{N_X!N_{Li}!}\frac{n!}{n_X!n_{Li}!}\right)$$

$$\frac{dF}{dN_X} = -\frac{dF}{dn_X},\ \frac{d\ln W}{dN_X} = \ln\frac{N-N_X}{N_X} - \ln\frac{n-n_X}{n_X} = \ln\left(\frac{N_{Li}n_X}{N_Xn_{Li}}\right)$$

$$\left(\frac{dF}{dn}\right)_T = 0.5(\gamma_{X-Li} + \gamma_{X-LLZO}) \times s_X - \gamma_{X-Li} \times s_X + kT\ln\left(\frac{N_{Li}n_X}{N_Xn_{Li}}\right) = 0$$

$$\ln\left(\frac{N_{Li}n_X}{N_Xn_{Li}}\right) = -\frac{0.5(\gamma_{X-LLZO} - \gamma_{X-Li}) \times s_X}{kT}$$

$$\frac{n_X}{n_{Li}} = \frac{N_X}{N_{Li}} \times e^{\left(-\frac{0.5(\gamma_{X-LLZO} - \gamma_{X-Li}) \times s_X}{kT}\right)} = \frac{N_X}{N_{Li}} \times e^{\left(-\frac{\Delta E}{kT}\right)}$$

For LiF, $\gamma_{LiF-LLZO} - \gamma_{LiF-Li} = -0.14\, J/m^2 < 0$ (Fig. S6)

$$\frac{n_{LiF}}{n_{Li}} \gg \frac{N_{LiF}}{N_{Li}}$$

LiF tends to concentrate in the interface of Li - LLZO.

For Li_9Al_4,

$\gamma_{Li_9Al_4-LLZO} - \gamma_{Li_9Al_4-Li} = 0.746\, J/m^2 > 0$ (Fig. S6)

$$\frac{n_{LiF}}{n_{Li}} \ll \frac{N_{LiF}}{N_{Li}}$$

Li_9Al_4 tends to be in the bulk of Li.

LLZO based interface energy analysis

Herein, nonstoichiometric Li-terminated (100) surface of $Li_7La_3Zr_2O_{12}$ is adopted.[49,50] The surface energy of LLZO is defined as:

$$\gamma = \frac{1}{2A}(E_{slab} - n_{formula}\mu_{bulk} - \sum n_i\mu_i)$$

where A is the cross-section area, E_{slab} is the total energy of the LLZO slab, $n_{formula}$ is the integer number of stoichiometric formula units in the slab, μ_{bulk} is the energy of one formula unit of corresponding bulk LLZO structure, n_i is the number of atoms of type i in the slab in excess of the stoichiometric amount. μ_i is the chemical potential of element i, which are described by the following equations,[51]

$$E_{La_2O_3} = 2\mu_{La} + 3\mu_O$$

$$E_{Li_6Zr_2O_7} = 6\mu_{Li} + 2\mu_{Zr} + 7\mu_O$$

$$E_{Li_8ZrO_6} = 8\mu_{Li} + \mu_{Zr} + 6\mu_O$$

$$E_{Li_{metal}} = \mu_{Li}$$

For LLZO based interface structures, the interface energies were evaluated as:

$$\gamma = \frac{1}{2A}(E_{inter} - E_{LLZO-slab} - E_{LiX}) + \gamma_{LLZO} + \gamma_{LiX}$$

Where E_{inter} is the total energy of the LLZO-LiX interface cell, E_{LLZO} and E_{LiX} are the energies of the isolated slab of this interface structure, γ_{LLZO} and γ_{LiX} are the surface energies of the isolated slab of this interface structure.

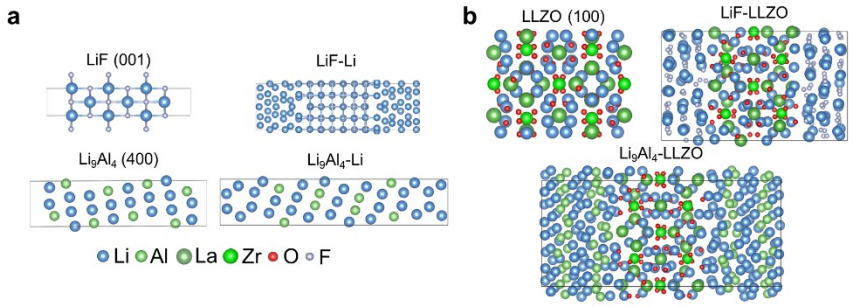

c

Configuration	Surface energy or interfacial energy (J/m²)
LiF (001)	0.32
LiF-Li	0.79
LiF-LLZO	0.65
Li_9Al_4 (400)	0.83
Li_9Al_4-Li	0.004
Li_9Al_4-LLZO	0.75

Figure S6. (a) Atomic structures for the Li_9Al_4 (400), LiF (001), Li_9Al_4–Li interface and LiF–Li interface. (b) The atomic structures of LLZO, LiF-LLZO interface and the Li_9Al_4 interface. (c) The corresponding surface and interfacial energies.

The Li-Al phase diagram

We then studied the Li-Al phase diagram to analyze the products formed by adding AlF_3 to molten Li. According to the first-principles computation results shown in Table S1, AlF_3 can totally react with Li at 300 °C when the Li/AlF_3 mass ratio reaches 1:2.30 and give LiF and Li_9Al_4 products. In the Li_9Al_4 product, the atomic percent of Li is 69.2%, which is pointed out using green dot in the Li-Al phase diagram of Figure S7. When the mass ratio of Li/AlF_3 increases to 2:1 and above, the Li-Al alloy phase in the composites become liquid, as labeled as purple, orange, blue dots, respectively. Actually, the phase diagram agrees well with our observation shown in Figure S4. Take the Li-AlF_3 composite with mass ratio of 2:1 as an example, there are LiF, Li_9Al_4 and excessive Li in the composite. Since the melting point of LiF is as high as 848.2 °C, LiF presents solid phase in the composite at 300 °C while Li-Al alloy is liquid. Thus, solid LiF would be excluded out from the liquid phase due to its lithiophobic nature. In the next cooling process, solid Li_9Al_4 phase gradually precipitates from Li-Al alloy. At last, a FGLA has been fabricated.

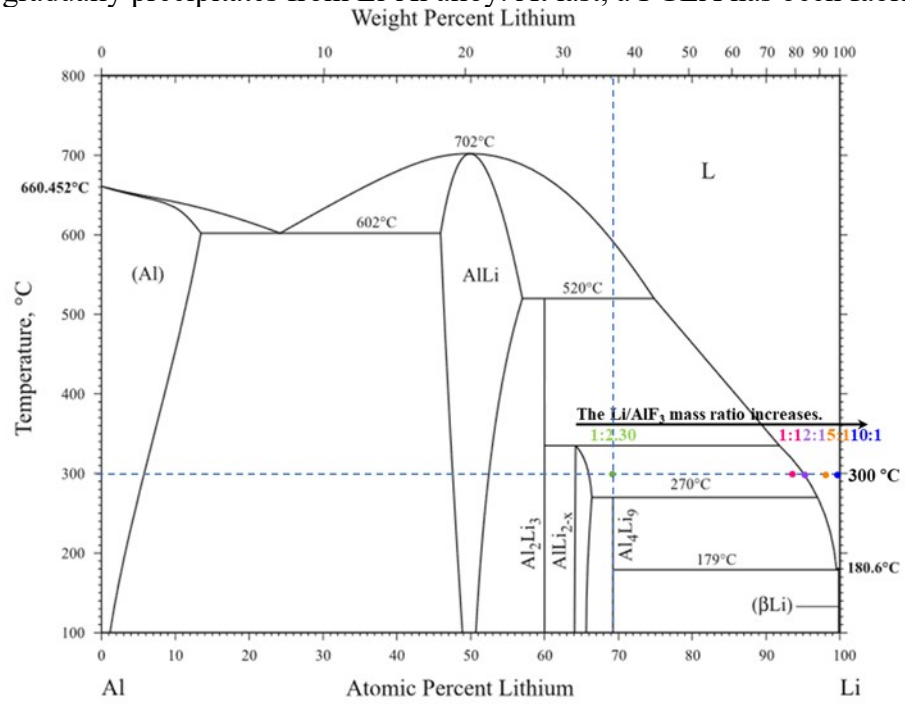

Figure S7. The phase diagram of Li-Al.

Phase separation process

As shown in Figure S8, pristine Li and FGLA were placed in stainless-steel containers on a hot plate (300 °C). The whole processes were carried out in an Argon-filled glovebox with the concentrations of moisture and oxygen < 0.1 ppm. There was no color change for pristine Li upon heating. On the other hand, the surface of FGLA presented metallic luster at the beginning. Interestingly, the surface turned grey after 5 s and then become dark after only 30 s. Depth-profiling XPS analysis and ToF-SIMS analysis confirmed that the newly formed dark layer was mainly LiF.

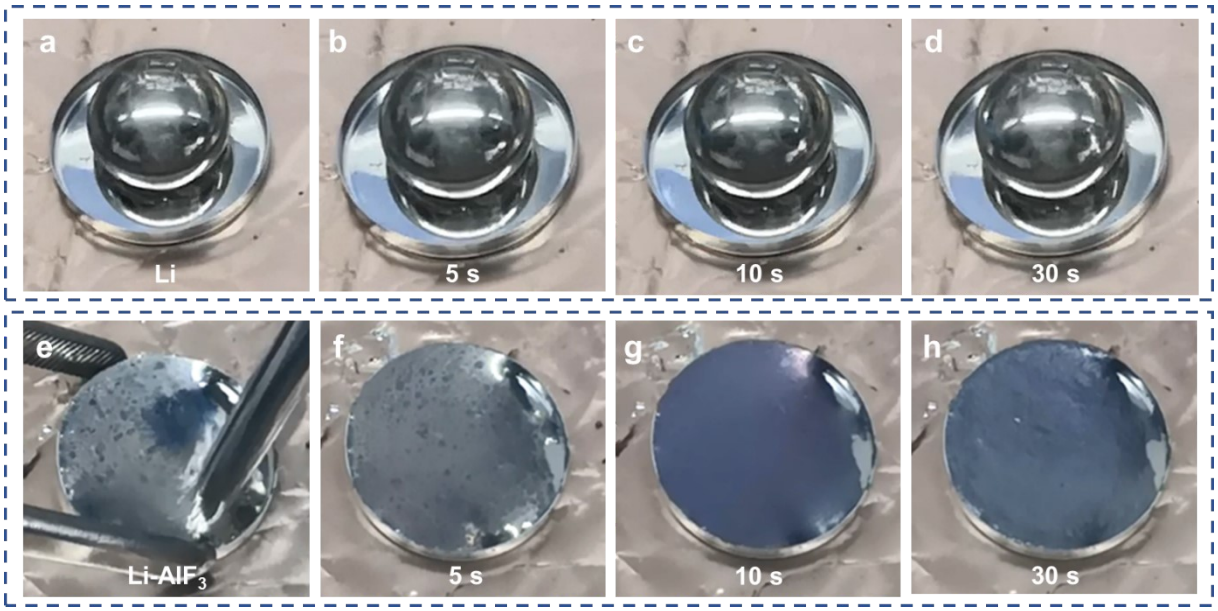

Figure S8. The surface evolution of pristine Li and FGLA on a hot plate (300 °C). (a-d) Digital photos of pristine Li on a hot plate (300 °C). There is no color change. (e-h) Digital photos of FGLA on a hot plate (300 °C). Clearly, a new layer of LiF is formed rapidly on the surface of FGLA.

XPS and ToF-SIMs characterizations

Surface chemical composition analysis was characterized using XPS (American Thermo Fisher Scientific ESCALAB 250Xi). The depth-profiling XPS analysis was conducted combining with Ar^+ ion sputtering. The sputtered thickness was determined by the sputtering time multiplied by sputtering speed (2.7 Å/s). The collected data were normalized.

ToF-SIMS analysis was taken using an instrument (IONTOF GmbH) from Münster, Germany, with a pulsed Ga^{3+} primary ion beam. A negative mode was conducted to detect the signal of F^-. The detected area is shown in Fig. S9.

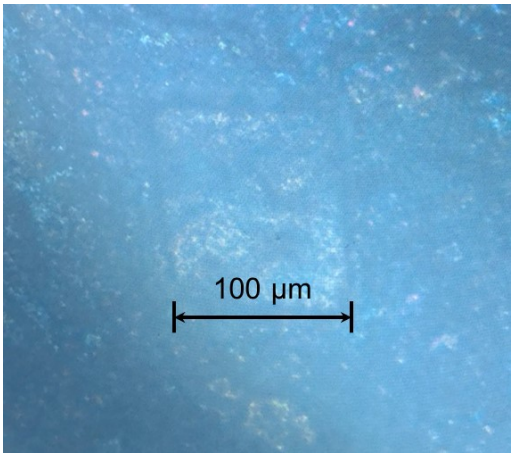

Figure S9. The digital photo of the sputtered area with depth-profiling ToF-SIMS. The area is about 100 by 100 µm.

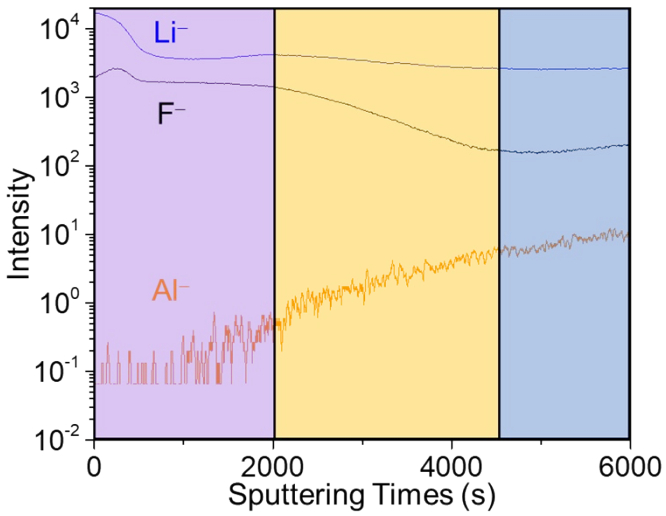

Figure S10. Depth-profiling TOF-SIMS of Li^-, F^- and Al^- secondary ion fragments conducted at the surface of FGLAs proved the gradient structure of FGLA.

X-ray photoelectron spectroscopy (XPS) combined with Ar^+ ion sputtering was applied to characterize the composition gradient structure. As shown in Fig. S11, the peak at ~685 eV in the F1s spectrum is ascribed to LiF.[2,30] Clearly, LiF shows a high and relatively stable intensity from the top surface and start to fade after 200 nm of depth, while the Al2p signal keeps a very low level and gradually increases after sputtering the top 200 nm and surpasses the LiF signal from 1200 nm. Fig. S10C shows the relative atomic concentration of LiF and Li_9Al_4 at different depth obtained from the spectra in Fig. S11A and Fig. S11B. A composition gradient at different thicknesses of the Li-AlF_3 composite demonstrated that LiF is rich in the surface layer of 200 nm and then amount of LiF quickly reduced after 200 nm. Between 200 to 1000 nm, both Li_9Al_4 and LiF mixed together. After 1000 nm, Li_9Al_4 concentration quickly increases in LiF-Li_9Al_4-Li composite. XPS characterization confirmed that the lithiophobic-lithiophilic gradient LiF-Li_9Al_4-Li composite (FGLA) was successfully formed by reacting of AlF_3 with molten Li.

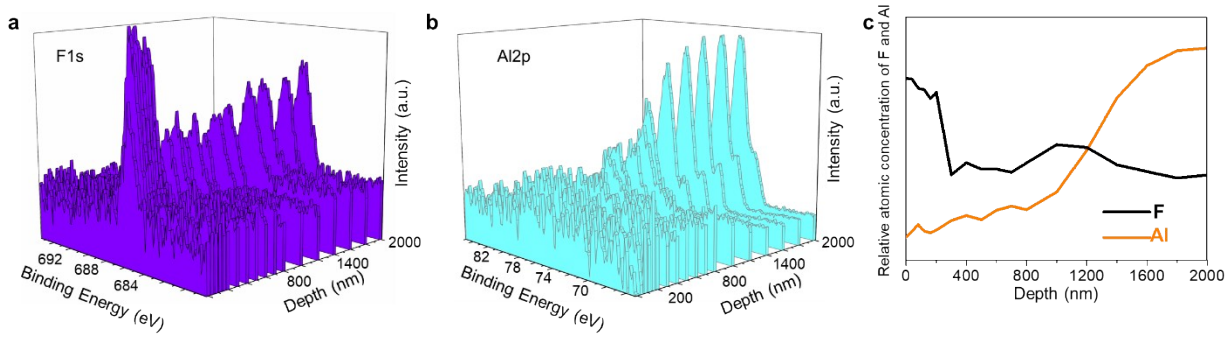

Figure S11. Depth-profiling XPS analysis with high-resolution XPS spectra of (a) F1s and (b) Al2p from the top surface to 2000 nm deep. (c) Relative atomic concentration of F and Al with depth.

The synthetic procedure and characterizations of LLZTO pellets.

In order to prepare LLZTO, the starting materials ($LiOH{\cdot}H_2O$, La_2O_3, ZrO_2 and Ta_2O_5) were milled with zirconia ball as well as isopropanol for 12 hours with a speed of 365 rpm and after drying were sintered at 900 °C for 12 hours. Next, the as-obtained powder was ball-milled with the same conditions mentioned above and then pressed into pellets after drying. Finally, the pellets were annealed at 1150 °C for 2 hours to be dense. To measure the ionic conductivity, both sides of LLZTO pellet were coated with Au. EIS profiles were conducted with an AC amplitude of 10 mV and a frequency ranging from 1000 kHz to 10 mHz.

The obtained LLZTO pellet was well polished, which showed a smooth surface, as shown in Fig. S12a. XRD pattern in Fig. S12b confirms that the as-prepared LLZTO pellet is cubic phase. The cross-section SEM image of LLZTO proves its dense structure (Fig. S12c). Fig. S12d and S12e show the EIS profiles and the corresponding Arrhenius plots of the as-obtained LLZTO pellet. The ionic conductivity of the LLZTO pellet is 5.06×10^{-4} S cm^{-1} at 25 °C and its active energy is about 0.33 eV.

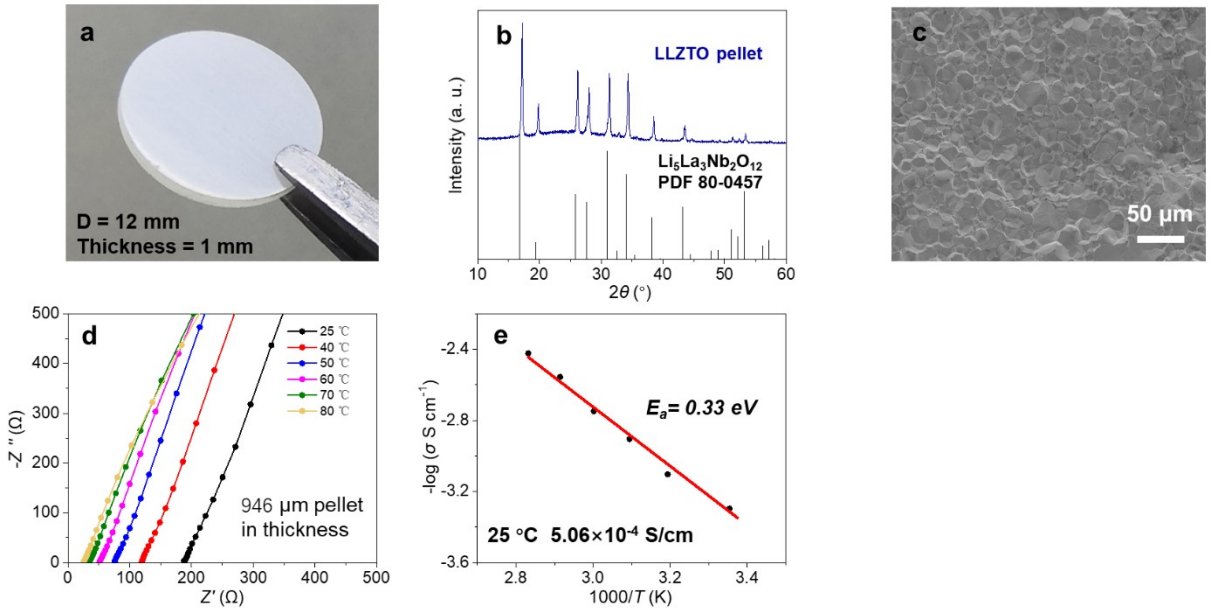

Figure S12. (a) A digital photo of a LLZTO pellet. (b) The XRD pattern of a LLZTO pellet and a standard $Li_5La_3Nb_2O_{12}$ with cubic garnet phase as reference. (c) A cross-sectional SEM image of LLZTO pellet. (d) EIS spectra of the as-prepared LLZTO pellet from 25 to 80 °C. (e) The Arrhenius plot of the LLZTO pellet.

The synthetic procedures and characterizations of LiAl alloy

Al foil was first cut into pieces and added into molten Li in a stainless-steel crucible at 300 °C under stirring. The mass ratio of Li/Al is 1:0.18. The Li/Al mass ratio in the LiAl alloy is the same as that in FGLA with a Li/AlF_3 mass ratio of 2:1. The XRD patterns of the Al foil, Li metal and the LiAl alloy were displayed in Fig. S13. We cannot detect signals from Al foil in LiAl, revealing the complete reaction of Al foil. The LiAl alloy was later used to measure the contact angle and assembly symmetric cells.

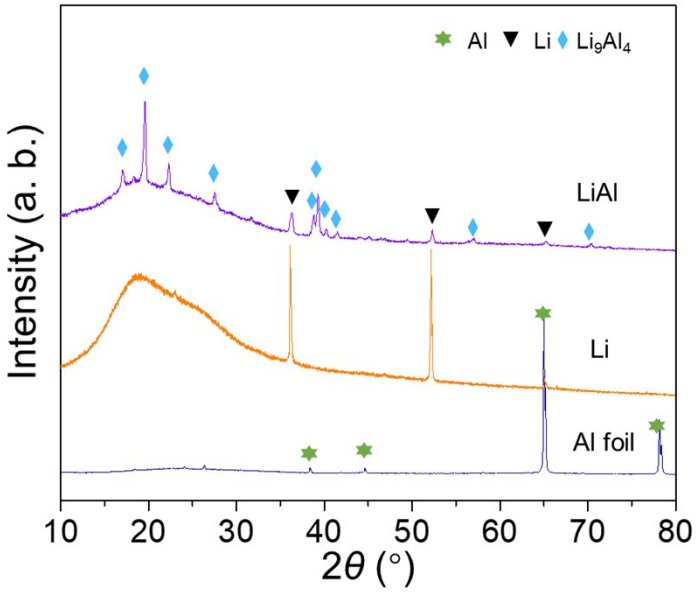

Figure S13. XRD patterns of LiAl alloy, Li metal and Al foil.

The synthetic procedures and characterizations of LiF-coated LLZTO

Before depositing LiF, LLZTO pellets were carefully polished. Then, a thin LiF layer (400 nm) was evaporated onto the LLZO pellet by an electron beam evaporation system (base pressure < 3 × 10^{-6} Torr). The deposition speed was calibrated with AFM to determine the coating thickness on Si wafer. In this study, a deposition rate of 0.1 Å/s was utilized to deposit a dense LiF layer. The deposition process was conducted for 40000 seconds to get a 400 nm thick layer of LiF.

The cross-sectional SEM images of LiF-coated LLZTO were shown in Fig. S14. A dense and homogeneous layer was seen. Furthermore, the EDX mapping profiles confirmed the uniform distribution of LiF (Fig. S15).

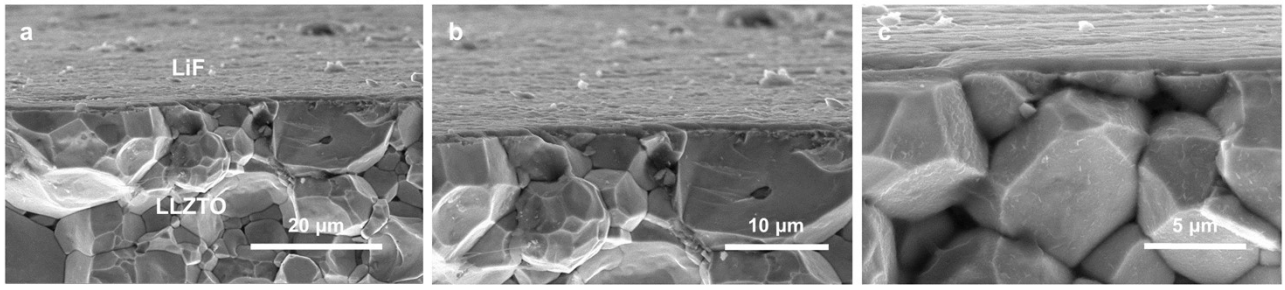

Figure S14. Cross-sectional SEM images of LiF-coated LLZTO.

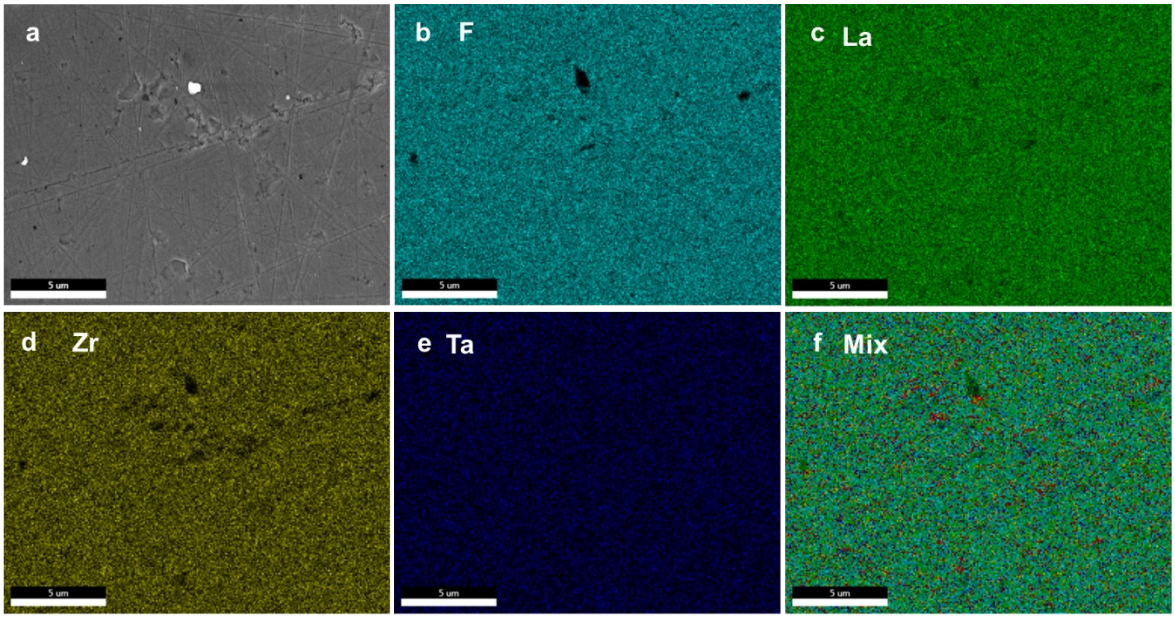

Figure S15. (a) The top view SEM image and elemental mappings of (b) F, (c) La, (d) Zr, (e) Ta and (f) mix of the LiF coated LLZTO pellet. The scale bar is 5 μm.

Wettability tests

(I) Contact angle tests

To evaluate the wettability of Li metal-based anodes with garnet, sessile drop tests were carried out. Li metal, LiAl alloy, or FGLA droplet was quickly deposited onto LLZTO or LiF-coated LLZTO pellets. The pellets were placed on a hotplate at 300 °C and the corresponding photos were taken to measure the contact angles.

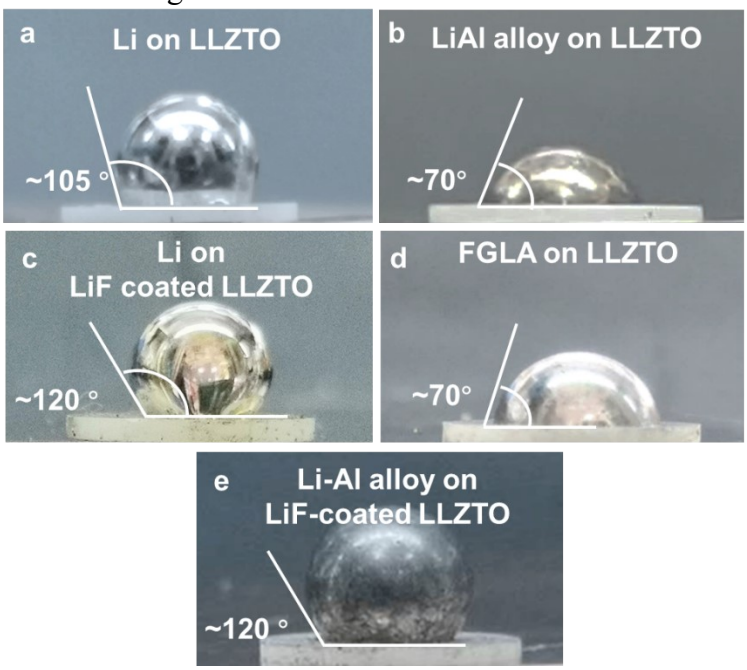

Figure S16. Interface wetting properties of various Li metal-based anodes with garnet-type $Li_{6.5}La_3Zr_{1.5}Ta_{0.5}O_{12}$ SSE. Photographs of (a) pure Li and (b) LiAl alloy droplets on smooth LLZTO SSE. A much better interface wetting was given by alloying Li with Al. (c) A photograph of Li droplet on LLZTO SSE coated with a thin layer of LiF, revealing the super-lithiophobicity of LiF. (d) A photograph of FGLA droplet on a smooth LLZTO SSE. (e) The photograph of LiAl alloy droplet on LiF-coated LLZTO. The large contact angle demonstrates that even LiAl alloy cannot wet garnet when a layer of LiF was deposited on garnet.

(II) SEM and EDX mapping images of Li/LLZTO interfaces

As displayed in Fig. S17, gaps exist in pure Li/LLZTO interface, indicating the poor wettability of Li metal to LLZTO. The gaps would result in the inhomogeneous distributions of current and formation of Li dendrite. In terms of pure Li on LiF-coated LLZTO, a much larger gap is observed, which is due to the superlithiophobicity of LiF to Li. In contrast, both LiAl alloy and FGLA composite can achieve close contacts with garnet. Since LiF is also existing in the FGLA composite, it is strongly proven that the *in-situ* formed LiF-rich layer does not worsen the interface contact.

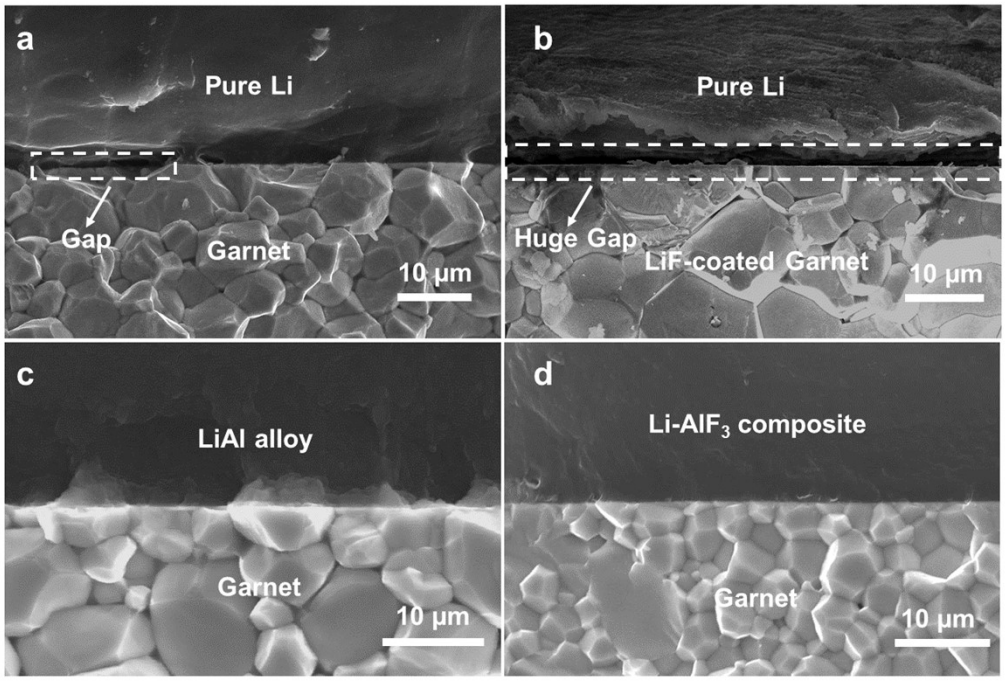

Figure S17. The cross-sectional SEM images of (a) Li/LLZTO interface. (b) Li/LiF-coated LLZTO interface. (c) LiAl alloy/LLZTO. (d) FGLA/garnet LLZTO.

Electrochemical performance measurement

(I) Symmetric cell tests

2032-type coin cells were used in this study with nickel foams as current collectors. The stacking pressures were ~3.4 MPa during cell assembly. We did not apply extra stress during cell testing and the pressure conditions for all cells were the same. To sandwich LLZTO by two FGLA electrodes, we prepared one side by one side. Typically, FGLA in a stainless-steel container was placed on a hot plate (300 °C) in an Ar-filled glovebox. Then, a LLZTO pellet was placed on the FGLA and rubbed in the container. After about 1 minute, one side of the LLZTO pellet was fully covered by FGLA. Then, another side was treated using the same method. After both sides were covered with FGLA, the sandwich structure was kept at 300 °C to form a self-regulated gradient interphase, followed by cooling down to room temperature and coin-cell assembling.

The Li|LiF-coated LLZTO|Li symmetric cell was sandwiched by two identical pure Li electrode at 300 °C. All procedures were carried out in a glove box filled with argon. An AC amplitude of 10 mV and a frequency from 1 MHz to 10 mHz were utilized to measure the EIS profiles of symmetric cells at 25 °C.

The critical current density was measured at 25 °C with gradually rising current densities (50, 100, 200, 300, 500, 800, 1000, 1200, 1500, 2000, 2400, 2600, 3000 μA/cm^2) and each charge/discharge step was fixed at 30 min. The CCD with a fixed capacity of 0.1 mAh/cm^2 was tested at RT with gradually rising current densities of 0.5, 1.0, 1.5, 2.0, 2.5, 3.0, 3.5, 4.0, 4.5, 5.0, 5.5, 6.0, 6.5, 7.0, 7.5, 8.0, 8.5, 9.0, 9.5, 10.0, 11.0, 12.0 and 12.7 mA/cm^2.

As for CCD tests at 60 °C, the capacity was fixed at 0.1 mAh/cm^2 with the stepwise current densities (1.0, 1.5, 2.0, 2.5, 3.0, 3.5, 4.0, 4.5, 5.0, 5.5, 6.0, 6.5, 7.0, 7.5, 8.0, 8.5, 9.0, 9.5, 10.0, 11.0, 12.0, 13.0, 14.0, 15.0, 16.0, 17.0, 18.0, 19.0, 20.0, 21.0, 22.0, 23.0, 24.0, 25.0 mA/cm^2).

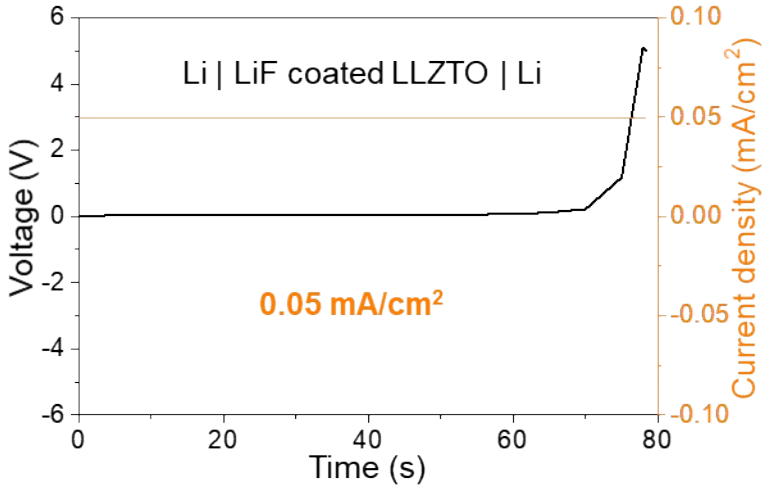

Figure S18. Galvanostatic cycling of a symmetric Li|LiF-coated LLZTO|Li cell at RT.

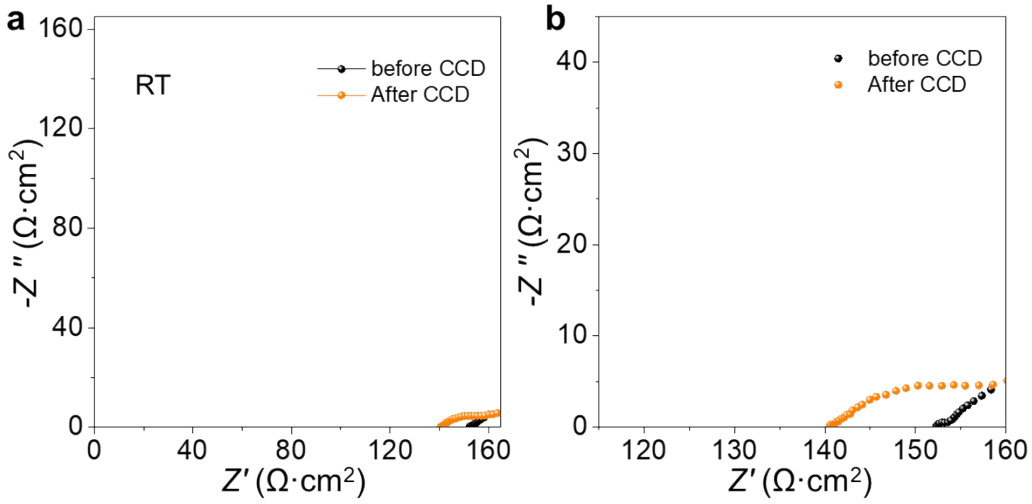

Figure S19. EIS patterns of FGLA|LLZTO|FGLA before and after CCD tests at RT.

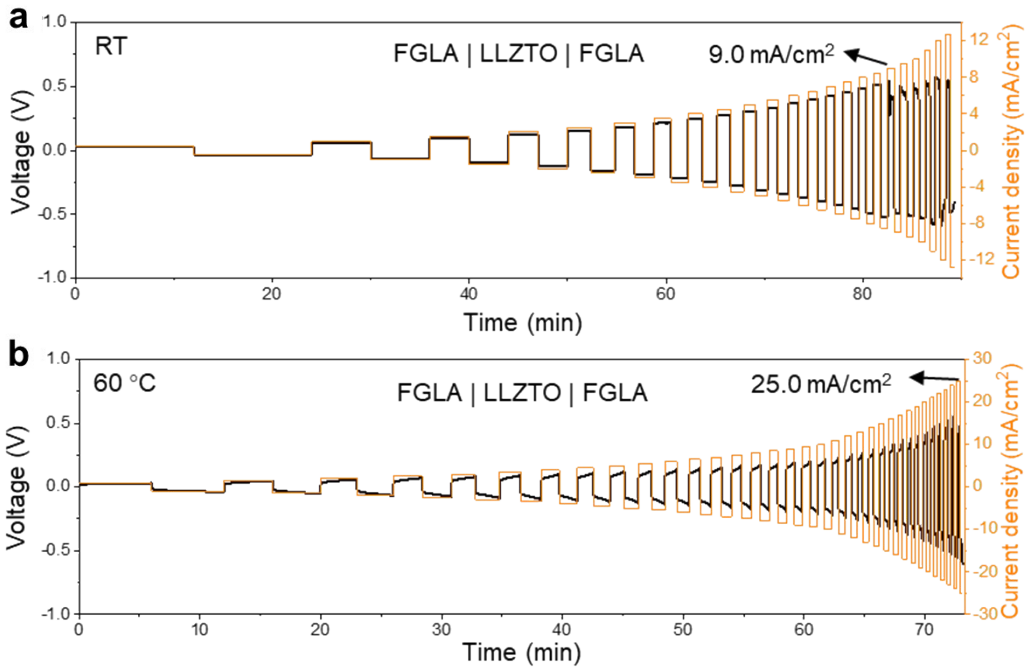

Figure S20. Galvanostatic cycling of symmetric FGLA|LLZTO|FGLA cells with a fixed capacity at RT and 60 °C. At a capacity of 0.1 mAh/cm^2, the CCD of FGLA|LLZTO|FGLA cells can be largely increased to 9 mA/cm^2 at RT and 25 mA/cm^2 at 60 °C.

(II) Full cell tests

To fabricate full cells, different cathodes were prepared, and 2032-type coin cells were used. NCM523 electrodes were prepared by mixing commercially available NCM523, carbon black and polyvinylidene fluoride (PVDF) binder with a mass ratio of 90:5:5 in N-methyl-2-pyrrolidinone (NMP) to form a slurry, which was then casted onto Al foil and dried at 90 °C under vacuum overnight. The S/C cathode was prepared via a simple freeze-drying method. 80 wt% sulfur/Kejten black was mixed with 10 wt% super P and 10 wt% LA133 binder. After being cast onto carbon-coated Al foil, the electrode was frozen to dry at – 20 °C under vacuum. The mass loading of sulfur was ~1.1 mg/cm^2. Thick LFP cathode was commercially available and the loading of LFP is ~2.8 mAh/cm^2.

To assemble Li|liquid|NCM523 full cells, celgard-2400 membranes and 60 µL electrolyte (1.0 M $LiPF_6$ in EC/DEC(v/v=1:1) with 10% FEC and 1% VC as additives) were used. In Li-S cells, the electrolyte is 1.0 M lithium bis(trifluoromethanesulfonyl)imide (LiTFSI) dissolved in tetraethylene glycol dimethyl ether (TEGDME) solvent with 0.1 M Li_2S and 0.1 M P_2S_5 as additives.[39] To assemble liquid Li-S full cells, 60 µL electrolyte was added with celgard-2400 separators. In Li|liquid|LFP full cells, 60 µL electrolyte (1.0 M $LiPF_6$ in EC/DEC(v/v=1:1) with 10% FEC and 1% VC as additives) was added with celgard-2400 separators. To assemble garnet-based full cells, the fabrication process of anode side was the same as that in symmetric cells and 15 µL electrolyte was dropped on the cathode side to wet the cathode/garnet interface.

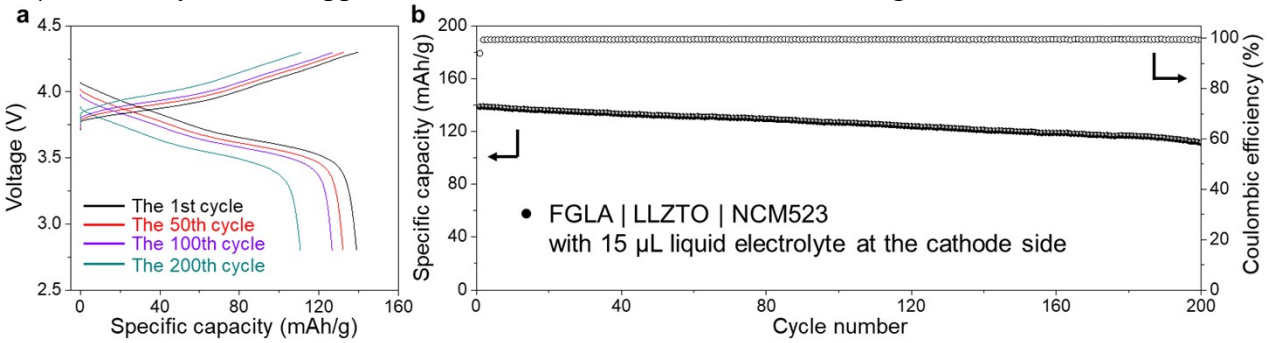

Figure S21. (a) Charge and discharge profiles of the FGLA|LLZTO|NCM523 cell at 2C (~1.3 mA/cm^2) and (b) the corresponding cycling performances. The mass loadings of NCM523 were about 4 mg/cm^2. 15 µL liquid electrolyte was added at the cathode side. The solid-state cell exhibits a capacity of 139 mAh·g^{-1} (0.53 mAh·cm^{-2}) at 2 C (1.3 mA·cm^{-2}) and retains ~80 % of the specific capacity after 200 cycles, which is highly improved compared to ~50 % for the liquid full cell. 15 µL liquid electrolyte was added at the cathode side.

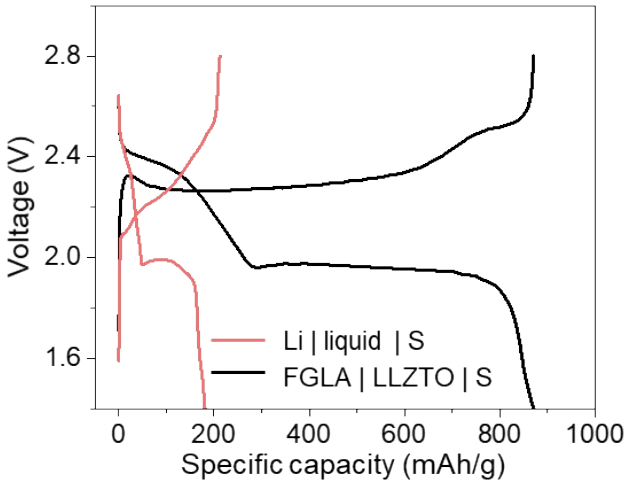

Figure S22. The 300th charge-discharge curves of the FGLA|LLZTO|S cell and the liquid Li-S cell. 15 μL liquid electrolyte was added at the cathode side.

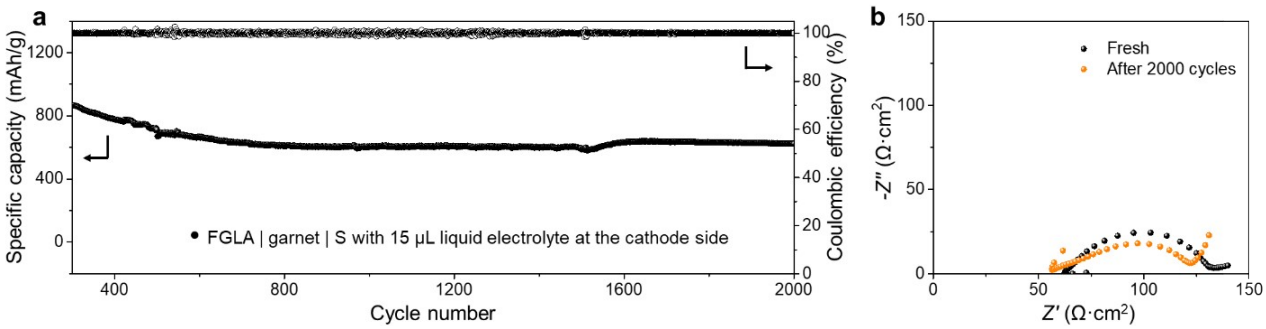

Figure S23. (a) The cycling performances of the FGLA|garnet|S cell from 301st-2000th cycle. And the FGLA|garnet|S cell can still deliver a discharge capacity of ~ 620 mAh/g after 2000 cycles. (b) The EIS profiles of the FGLA|garnet|S cell before and after 2000 cycles, showing an ultra-stable interface. 15 μL liquid electrolyte was added at the cathode side.

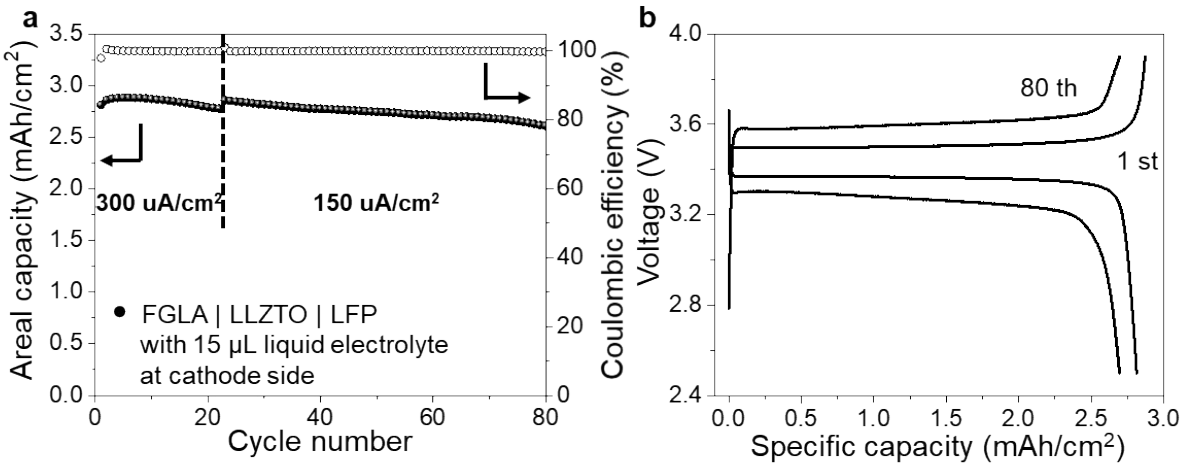

Figure S24. (a) The cycling performance of the FGLA|LLZTO|LFP cell and (b) the charge-discharge curves of the FGLA|LLZTO|LFP cell at specific cycles. The areal capacity of LFP cathode is about 2.83 mAh/cm^2. 15 µL liquid electrolyte was added at the cathode side.

Table S1. Possible reactions between Li metal and AlF_3. The corresponding data were from the Materials Project (MP) (*38*).

Molar Fraction	Mass ratio Li: AlF_3	Reaction Equation (normalized to reflect molar fraction)	E_{rxn} of eqn (kJ/mol)	E_{rxn} / atom (eV/atom)
0.000		/	/	/
0.160	1: 2.30	$0.84\ Li + 0.16\ AlF_3 \rightarrow 0.04\ Li_9Al_4 + 0.48\ LiF$	-62.24	-0.436
0.167	1: 2.426	$0.833\ Li + 0.167\ AlF_3 \rightarrow 0.167\ Li_2Al + 0.5\ LiF$	-64.57	-0.446
0.182	1: 2.692	$0.818\ Li + 0.182\ AlF_3 \rightarrow 0.091\ Li_3Al_2 + 0.545\ LiF$	-69.79	-0.468
0.200	1: 3.025	$0.8\ Li + 0.2\ AlF_3 \rightarrow 0.2\ LiAl + 0.6\ LiF$	-74.91	-0.485
0.250	1: 4.033	$0.75\ Li + 0.25\ AlF_3 \rightarrow 0.75\ LiF + 0.25\ Al$	-84.98	-0.503
0.400	1: 8.066	$0.6\ Li + 0.4\ AlF_3 \rightarrow 0.2\ Li_3AlF_6 + 0.2\ Al$	-74.70	-0.352
1.000		/	/	/

Table S2. Composition and capacity calculations of FGLA with different Li/AlF_3 mass ratios.

Sample	Compositions	Li: Al: F atom ratios	Li: Li_9Al_4: LiF mole ratios	Capacity calculation/ mAh/g
Li:AlF_3=1:2.30	AlF_3, Li_9Al_4, Li_3Al_2, LiF	5.2:1:3	0:1:12	0
Li:AlF_3=1:1	Li, Li_9Al_4, LiF	12:1:3	27:1:12	1086
Li:AlF_3=3:2	Li, Li_9Al_4, LiF	18:1:3	51:1:12	1641
Li:AlF_3=2:1	Li, Li_9Al_4, LiF	24:1:3	75:1:12	2016
Li:AlF_3=5:1	Li, Li_9Al_4, LiF	60:1:3	219:1:12	2935
Li:AlF_3=10:1	Li, Li_9Al_4, LiF	120:1:3	459:1:12	3356
Pure Li	/	/	/	3861

Table S3. Comparisons of critical current densities (CCDs) for garnet-based Li||Li symmetric cells.

SSE type	Methods	Testing temperature	Critical current density/ (mA/cm^2)	References
Garnet	PECVD Si	25 °C	0.2	J. Am. Chem. Soc. 138, 12258-12262 (2016)
Garnet	ALD Al_2O_3	25 °C	0.2	Nat. Mater. 16, 572-579 (2017)
Garnet	Sputtering Al	25 °C	0.2	Sci. Adv. 3, e1601659 (2017)
Garnet	Heating treatment	25 °C	0.3	Chem. Mater. 29, 7961-7968 (2017)
Garnet	Li_3N coating	25 °C	0.1	Nano Lett. 17, 565 (2017)
Garnet	LiAl alloy	25 °C	0.9	J. Mater. Chem. A 6, 18853-18858 (2018)
		60 °C	2.3	
Garnet	Drawing a graphite interface	25 °C	0.3	ACS Energy Lett. 3, 1212-1218 (2018)
		80 °C	0.5	
Garnet	Li-C composite	60 °C	1	Adv. Mater. 31, 1807243 (2019)
Garnet	Li-Mg alloy	25 °C	2	Adv. Mater. 31, 1804815 (2019)
Garnet	MoS_2	100 °C	2.2	Energy Environ. Sci. 12, 1404-1412 (2019)
Garnet	Optimizing microstructure	Room temperature	0.9	J. Power Sources. 31, 314-318 (2018)
		60 °C	6.0	
Garnet	Lithiophilic-lithiophobic FGLA	25 °C	>3 (without short-circuit)	**This work**
		60 °C	25.0 (without short-circuit)	

Table S4. Comparisons of mass loading and cycling performances for garnet-based LFP||Li full cells.

SSE type	Mass loading mg/cm^2	Areal capacity mAh/cm^2	Cycling performances	References
Garnet	2.0	0.3	100 cycles ~90.0 % capacity retention	Nano Lett. 18, 7414-7418 (2018)
Garnet	5.0	0.79	100 cycles ~98.8 % capacity retention	J. Mater. Chem. A 6, 18853-18858 (2018)
Garnet	1.0	0.14	100 cycles ~80.4 % capacity retention	Sci. Adv. 3, e1601659 (2017)
Garnet	5.0	0.75	50 cycles ~91.7 % capacity retention	Angew. Chem. Int. Ed. 59, 12069-12075 (2020)
Garnet	1.0	0.15	400 cycles ~88.0 % capacity retention	Adv. Mater. 32, 200030 (2020)
Garnet	3.0	0.42	50 cycles ~94.4 % capacity retention	J. Am. Chem. Soc. 140, 6448-6455 (2018)
Garnet	18.0	~ 2.85	80 cycles ~93.0 % capacity retention	**This work**

References

49. P. Canepa, J. A. Dawson, G. S. Gautam, J. M. Statham, S. C. Parker and M. S. Islam, *Chem. Mater.*, 2018, **30**, 3019–3027.
50. H. K. Tian, B. X. and Y. Qi, *J. Power Sources*, 2018, **392**, 79–86.
51. T. Thompson, S. Yu, L. Williams, R. D. Schmidt, R. G. Mendez, J. Wolfenstine, J. L. Allen, E. Kioupakis, D. J. Siegel and J. Sakamoto, *ACS Energy Lett.*, 2017, **2**, 462–468.